6th European Conference on Computational Mechanics (ECCM 6)
7th European Conference on Computational Fluid Dynamics (ECFD 7)
11 – 15 June 2018, Glasgow, UK

EFFET OF INTERFACIAL TRANSITIONAL ZONES ON CONCRETE BEHAVOUR IN DEM ANALYSES

MICHAL NITKA AND JACEK TEJCHMAN

Faculty of Civil and Environmental Engineering
Gdańsk University of Technology
Narutowicza 11/20, 80-233 Gdańsk, Poland
e-mail: micnitka@pg.edu.pl, tejchmk@pg.edu.pl

Key words: Concrete, Fracture, Aggregate, Cement matrix, ITZ, DEM.

Abstract. This paper presents 2D numerical studies on concrete fracture at the aggregate level by means of the discrete element method (DEM). Three-point quasi-static bending tests with notched beams were performed. Meso-structure of concrete was determined with x-ray micro-tomography. Concrete was described as a four phase material composed of aggregate, cement matrix, macro-voids and interfacial transitional zones (ITZs) between aggregates and cement matrix. ITZs were the weakest phase of concrete due to their high porosity and attracted a discrete macro-crack during fracture. Attention was laid on the impact of ITZs on the concrete behaviour. ITZ were modelled as porous zones with a defined thickness. A satisfactory agreement between calculations and experiments was achieved.

1 INTRODUCTION

Fracture in brittle materials (i.e. concrete) is the fundamental phenomenon in concrete materials [1-3]. It is a very complex process, composed of micro-cracks, secondary cracks and macro-cracks with various branches. Concrete has a very complicated heterogeneous structure over many different length scales (from few nanometres to millimetres). At the meso-scale concrete may be considered as a composite material that includes 4 important phases: cement matrix, aggregate, interfacial transitional zones (ITZs) and macro-voids [4-5]. In concrete, ITZs are the weakest phase due to their very porous structure [6-7]. The thickness of ITZs varies between 0 and 50 μm, depending upon the aggregate roughness. ITZs cannot be neglected in calculations since a discrete macro-crack is created through bridging interfacial micro-cracks. The concrete behaviour at the meso-level may be described with different numerical models within continuum [4,5,8] and discrete mechanics [9-13]. In this calculations used the classical particle discrete elements method (DEM). The 3D images from x-ray micro-computed tomography were used to generate the concrete meso-structure in DEM [13]-[16]. The open-source three-dimensional spherical discrete element code YADE [17-18] was used for numerical calculations. A simply linear contact under compression was used. The normal and tangential contact forces satisfied the cohesive-frictional Mohr-Coulomb condition. The method was very successful in describing fracture in concrete at both the macro- and meso-scale [13-16].

2 EXPERIMENTS

Three-point bending tests were carried out [14, 15]. Usual concrete was used, composed of ordinary Portland cement, gravel, sand and water. The mean aggregate diameter was d_{50}=2 mm and the maximum aggregate diameter was d_{max}=16 mm. The specimen was filed with 75% of aggregate in volume. The beam dimensions were equal: height = 80 mm, length = 320 mm and thickness = 40 mm. The notch of the height of 8 mm and width of 3 mm was located at the mid-span of the beam. Quasi-static tests with concrete beam under bending were performed with a controlled notch opening displacement rate (crack mouth opening displacement (CMOD)) of 0.002 mm/min using Instron 5569. The CMOD gauge with the length of 5 mm was located in the notch at the beam bottom. The test ended for CMOD=0.1 mm. The maximum vertical force F was equal to 2.15 kN (the tensile strength was 3.73 MPa). After the test, the beam mid-part (height 80 mm, width 50 mm and depth 40 mm) was cut out and placed inside the x-ray micro-tomograph device Skyscan 1173 [19]. The method allowed to precisely detect fracture of a heterogeneous complex 3D concrete meso-structure and to separate 3 phases (aggregates, cement matrix and macro-voids) (Fig.1a). The width of ITZs was determined with the scanning electron microscope Hitachi TM3030. The width changed between 30-50 μm (Fig.1b). The crack was strongly curved mainly due to presence of aggregates with ITZs (Fig.1a). Its shape changed along the specimen depth. It might rarely propagated through a weak aggregate particle and a macro-void [15]. The macro-crack was created by bridging the interfacial micro-cracks.

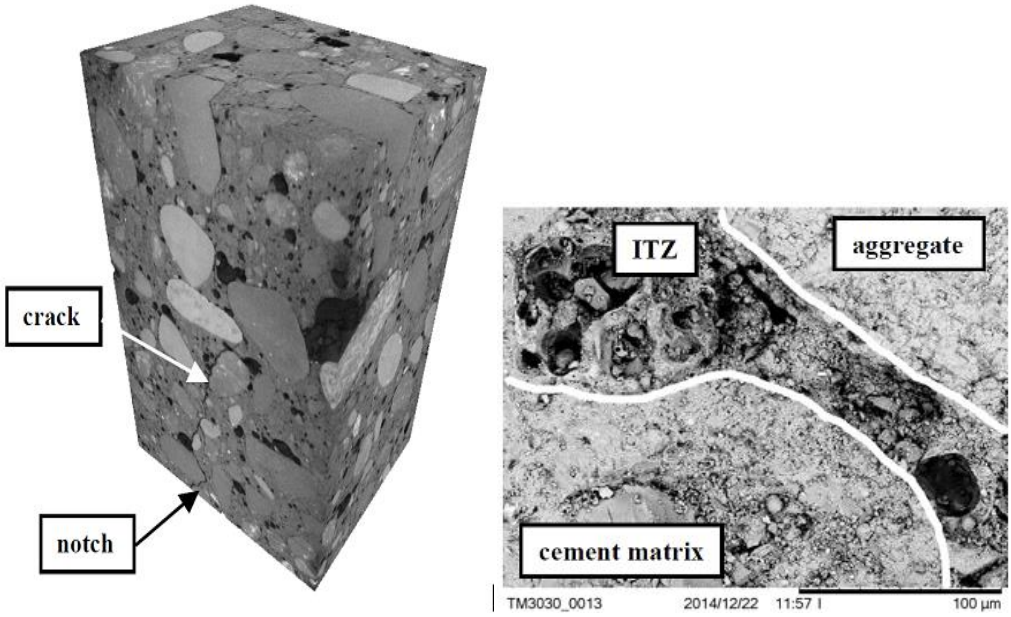

a) b)

Figure 1: a) General view on cut-out cracked cuboidal specimen 80×50×40 mm^3 obtained by means of 3D μCT and b) typical image of ITZs around aggregate in concrete specimen by means of scanning electron microscope

3 DISCRETE ELEMENT METHOD

The local contact deformation was modelled as a particle overlap (so-called soft-particle approach). The interaction force vector between two spherical discrete elements in contact was decomposed into a normal and tangential vector, respectively. The normal forces acting on spheres were modelled by an elastic law with cohesion. The normal and tangential forces were linked to the displacements through the normal stiffness K_n and the tangential stiffness K_s (Figs.2a and 2b) [17]:

$$\vec{F}_n = K_n U \vec{N}, \tag{1}$$

$$\vec{F}_s = \vec{F}_{s,prev} + K_s \Delta \vec{X}_s, \tag{2}$$

where U is the overlap between spheres, $\vec{N}$ is the normal vector at the contact point, $\Delta \vec{X}_s$ is the increment of the relative tangential displacement and $\vec{F}_{s,prev}$ is the tangential force from the previous iteration. The stiffnesses were computed as the functions of the modulus of elasticity of the grain contact E_c and two neighbouring grain radii R_A and R_B (to determine the normal stiffness K_n) and the modulus of elasticity E_c and Poisson's ratio υ_c of the grain contact and two neighbouring grain radii R_A and R_B (to determine the tangential stiffness K_s), respectively [17]:

$$K_n = E_c \frac{2R_A R_B}{R_A + R_B}, \qquad K_s = \nu_c E_c \frac{2R_A R_B}{R_A + R_B}. \tag{3}$$

A simple linear elastic contact law was assumed in normal contacts. The contact forces $\vec{F}_s$ and $\vec{F}_n$ satisfied the cohesive-frictional Mohr-Coulomb equation (Fig.2c)

$$\left\|\vec{F}_s\right\| - F_{max}^s - \left\|\vec{F}_n\right\| \times tan\,\mu \leq 0 \quad \text{(before contact breakage)}, \tag{4}$$

$$\left\|\vec{F}_s\right\| - \left\|\vec{F}_n\right\| \times tan\,\mu \leq 0 \quad \text{(after contact breakage)}, \tag{5}$$

where μ denotes the inter-particle friction angle and F_{max}^s is the cohesive force between elements. The normal force might be negative down to the minimum value of F_{min}^n (tension) if there was no a geometrical contact between elements. If this minimum normal force between spheres F_{min}^n was reached, the contact was broken. Moreover, if any contacts between grains re-appeared, cohesion between them was not taken into account. A crack was considered as open if cohesive forces between grains (Eq.4) disappeared when a critical threshold was reached. A choice of a very simple constitutive law was intended to capture on average various contact possibilities in real concrete. The cohesive force and tensile force were assumed as a function of the cohesive stress C (maximum shear stress at pressure equal to zero), tensile normal stress T and sphere radius R [20]:

$$F_{max}^s = CR^2 \qquad \text{and} \qquad F_{min}^n = TR^2. \tag{6}$$

For two elements in contact, the smaller values of C, T and R were used. A local non-viscous damping scheme was applied [21] in order to dissipate excessive kinetic energy in a discrete system. The following five main local material parameters were needed for our discrete simulations: E, υ, μ, C and T which may be successfully calibrated with real laboratory tests on uniaxial compression and uniaxial tension [13-16]. In addition, the particle radius R, particle mass density ρ and damping parameters α_d were required. Note that material softening was not assumed in the model. In DEM computations, concrete was described as a four-phase material that consisted of aggregate, cement matrix, ITZs and macro-voids. The cement matrix was simulated with spheres with the diameter 0.25-2 mm that filled the

specimen in 97% (as in experiments). Macro-voids were described as empty spaces. Aggregate was simulated as a cluster composed of small spheres (0.5 mm) connected to each other as rigid bodies. Each cluster might include 10-500 spheres. The mid-part of the beam was modelled as the four phase concrete only. The remaining beam region (outside the meso-region close to the notch) was simulated with spheres of d=2-8 mm (Fig.3a). The ITZs were inserted around all aggregates (Fig.3b). The ITZs were assumed as the mortar zones with a higher porosity (in contrast with our previous calculations wherein ITZs had no a physical thickness [13-16]). ITZs included 1, 2 or 3 layers of spheres with the diameter of 0.25-0.5 mm (Fig.3c).

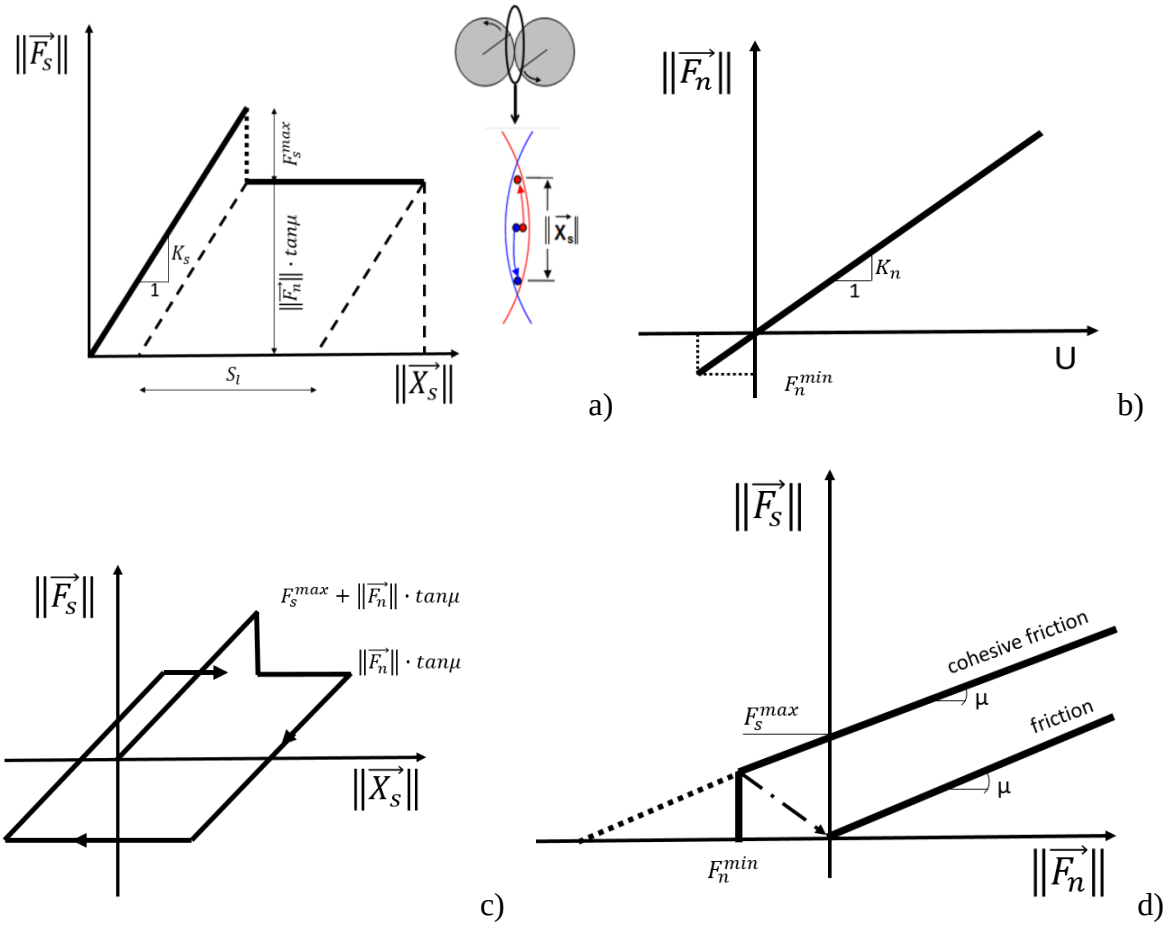

Figure 2: Mechanical response of DEM:
a) tangential contact model, b) normal contact model, c) loading and unloading path in tangential contact model and d) modified Mohr-Coulomb model

The following parameters were used in all calculations: $E_{c,cm}$=11.2 GPa, C_{cm}=140 MPa and T_{cm}=25 MPa. The detailed calibration procedure was described by Nitka and Tejchman [13]. The cement matrix and ITZs had the same parameters. In the remaining region outside the meso-region with large grains was described by the parameters: E_{macro}=12.8 GPa, C_{macro}=140 MPa and T_{macro}=25 MPa [14, 15]. The contact elastic stiffness of the cement

matrix and beam macro-zone were directly taken from the laboratory tests. The remaining parameters were: υ_c=0.2 (Poisson's ratio of grain contact), μ=18^o (inter-particle friction angle), α_d=0.08 (damping parameter) and ρ=2.6 kG/m^3 (mass density). The prescribed damping parameter and velocity did not affect the results. The calculated nominal inertial number I (which quantifies the significance of dynamic effects) was <10^{-3} that always corresponded to a quasi-static regime. The beam included in total about 40'000 spheres (35'000 elements in the meso-region).

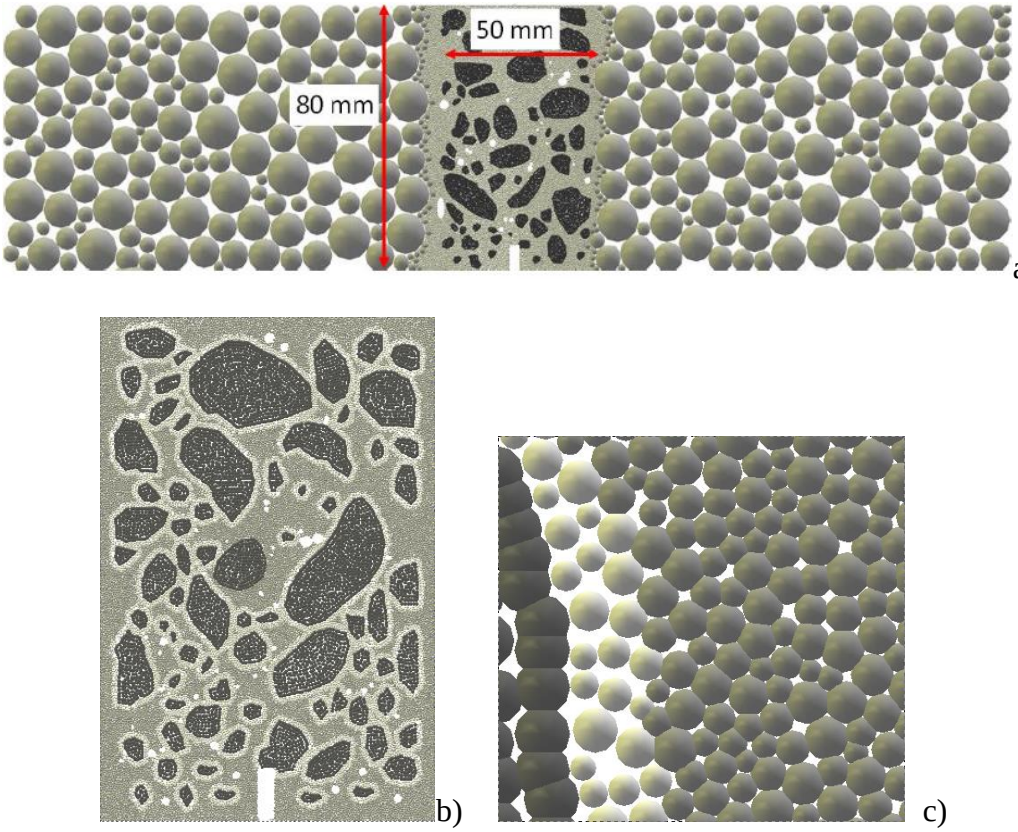

Figure 3: 2D geometry of the: a) entire beam and b) meso-region and c) zoom on ITZ (initial micro-porosity of 25% with 3 layers) (dark grey colour corresponds to aggregate, grey corresponds to cement matrix and light grey corresponds to ITZs)

4 NUMERICAL RESULTS

Two different methods were used due to generate the specimen structure with the defined initial porosity. In the first method, the entire specimen was prepared with the defined porosity. The layers around aggregates were next blocked (one, two or three) and the rest of spheres was removed. Later the specimen was filled with the cement matrix up to 3% of porosity. Thus the higher porosity was obtained around aggregates. In the second method, the specimen was created with a dense cement matrix in the entire area (porosity 3%). Next, the diameters of spheres close to aggregates (in 1, 2 or 3 layers) were decreased down to the value

that corresponded to initial porosity. In both cases all internal forces (due to overlapping) were removed before simulations.

Figure 4 shows the macroscopic results of the curve of the vertical force versus CMOD) from DEM as compared to the experimental one. The numerical results show good agreement with the experimental data for initial porosity of 20%. The maximum calculated vertical force was equal to F=2.20 kN for CMOD=0.02 mm with the specimen generation method '1' and F=2.20 kN for CMOD=0.023 mm with the specimen generation method '2' (in the experiment: F=2.18 kN for CMOD=0.017 mm). The computed residual force (CMOD=0.1 mm) was by about 50% and 100% higher than in the laboratory test. The generation method '1' indicated better agreement with the experiment, however was more time consuming. With increasing porosity both the maximum strength and global stiffness decrease. In Figure 5, the influence of the layer number in ITZs was shown for the generation method '1' (Fig.5A) and generation method '2' (Fig.5B). With increasing number of ITZ-layers, the force peak, stiffness and brittleness decreased.

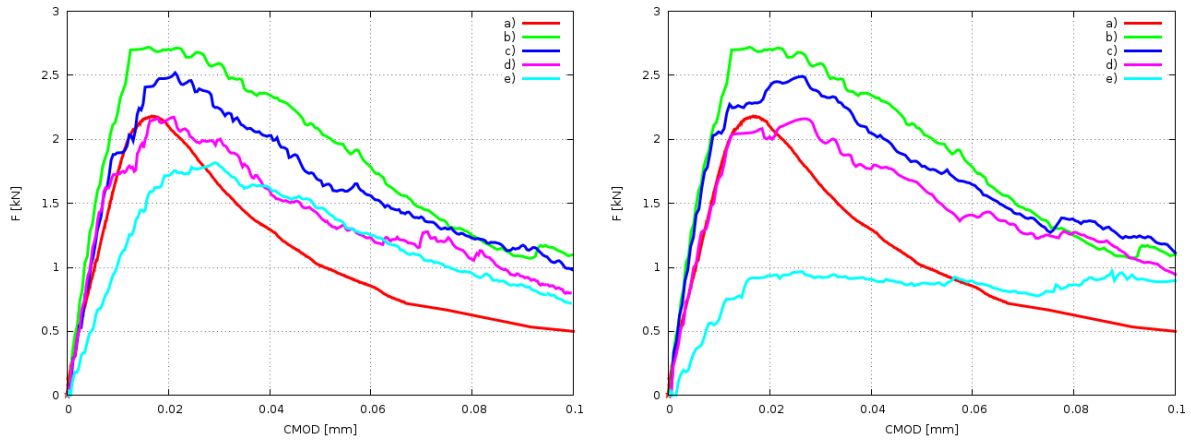

A) B)

Figure 4: Evolution of vertical force F against displacement CMOD in beam under 3-point bending for: A) specimen generation method '1' with ITZ porosity of: b) 3%, c) 10%, d) 20% and e) 25%) and B) specimen generation method '2' with ITZ porosity of: b) 3%, c) 12%, d) 22% and e) 30%) 'a' - experimental curve)

The numerical and experimental final crack path in the vertical cross-section was shown for CMOD=0.1 mm in Fig.6. The calculated crack path was similar as in the experiment. It propagated in ITZs around aggregates. It was affected by the presence of macro-voids. The calculated length of the discrete macro-crack was about 50 mm and was the same as in the experiment (about 75% of the specimen height).

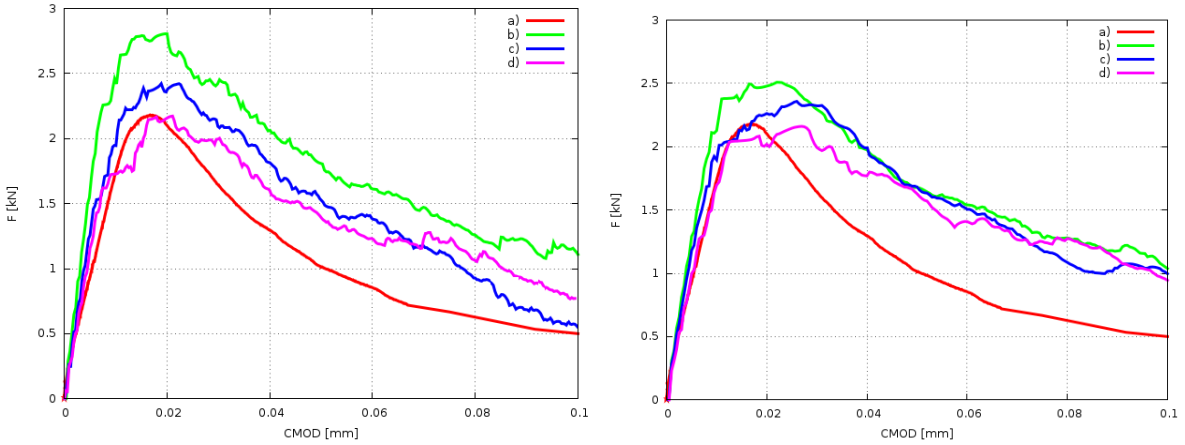

Figure 5: Evolution of vertical force *F* against displacement CMOD in beam under 3-point bending for: A) specimen generation method '1' with ITZ porosity of 22%: b) 1 ITZ-layer, c) 2 ITZ-layers and d) 3 ITZ-layers) and B) specimen generation method '2' with ITZ porosity of 22%: b) 1 ITZ-layer, c) 2 ITZ-layers and d) 3 ITZ-layers) ('a' - experimental curve)

Figure 7 presents the influence of ITZs on the crack shape. For the specimen with no ITZs (Fig.7a), the crack was straight. With increasing porosity in ITZs, the crack started to bend and its shape was more similar as in experiment. The best agreement was found for initial porosity of 20% (Fig.7c). With a very high porosity (30%), the macro-crack did not form, only micro-cracks appeared in the entire specimen (Fig.7Bd).

The influence of the number of ITZ-layers is presented in Fig.8. One ITZ- layer did not affect the crack path that was almost straight. Two ITZ-layers improved the crack shape for the specimen generation method '1' only. For 3 ITZ-layers, both the generation methods showed realistic results.

5 CONCLUSIONS

The following conclusions may be derived based on our DEM calculation outcomes:

ITZs extremely strongly affected the shape and length of the discrete macro-crack. The crack was shorter in length and more straight with low porosity of ITZs. The beam strength and stiffness were close to laboratory test for 3 layers of ITZ spheres with porosity of 20%. The macro-crack was always curved due to a stochastic distribution of aggregates. It possessed many small branches. The single micro-cracks also occurred far beyond the macro-crack. The shape of the crack was similar as in experiment (with respect to both the length and curvature).

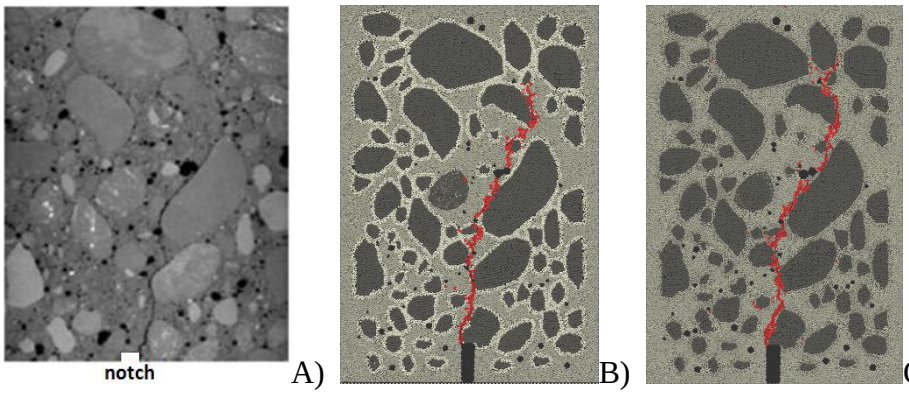

Figure 6: Final crack trajectory in concrete beam above notch after test for CMOD=0.1 mm: a) μCT-image, b) generation method '1' (3 layers of ITZ with 20%-porosity) and generation method '2' (3 layers of ITZ with 22%-porosity) (red colour denotes elements with broken contacts, dark grey - aggregate, light grey – ITZ, grey - cement matrix and black – macro-voids)

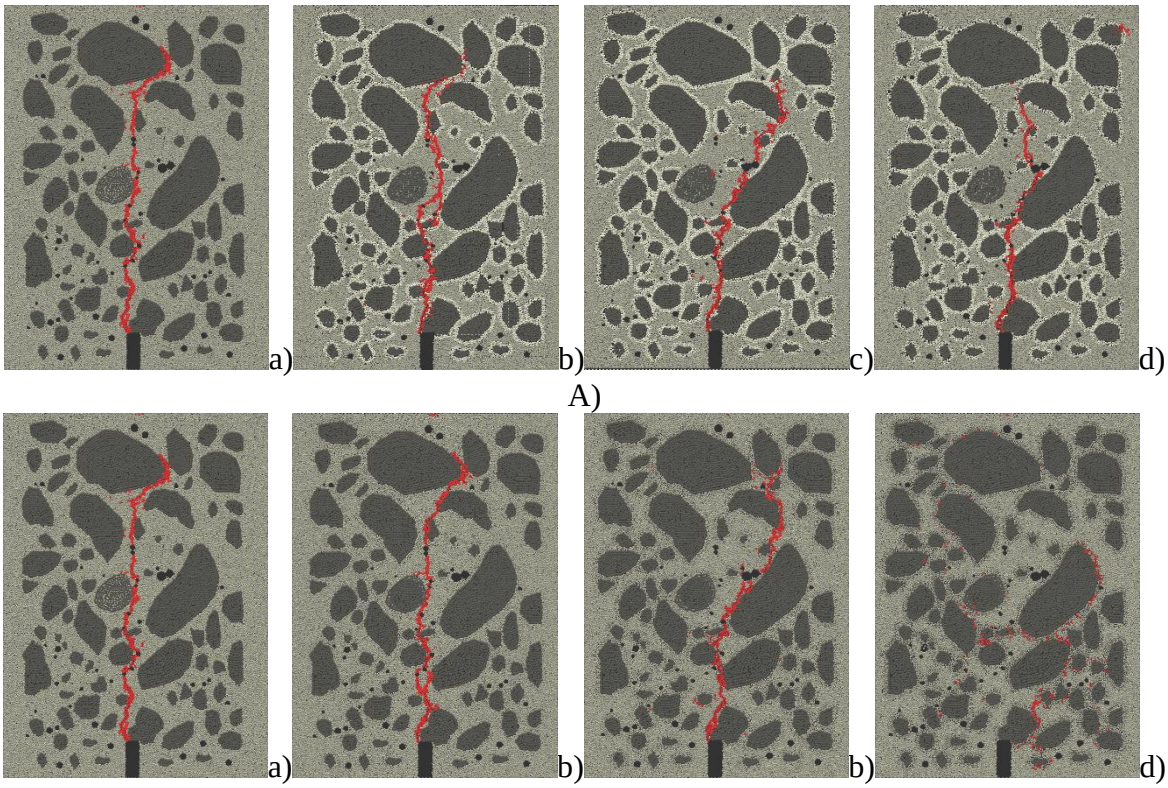

Figure 7: Final crack trajectory in concrete beam above notch after test for CMOD=0.1 mm: A) generation method '1' (3 ITZ-layers with porosity of: a) 3%, b) 10%, c) 20% and d) 25%) and B) generation method '2' (3 ITZ-layers with porosity of a) 3%, b) 12%, c) 22% and d) 30%) (red colour denotes elements with broken contacts, dark grey - aggregate, light grey – ITZ, grey - cement matrix and black – macro voids)

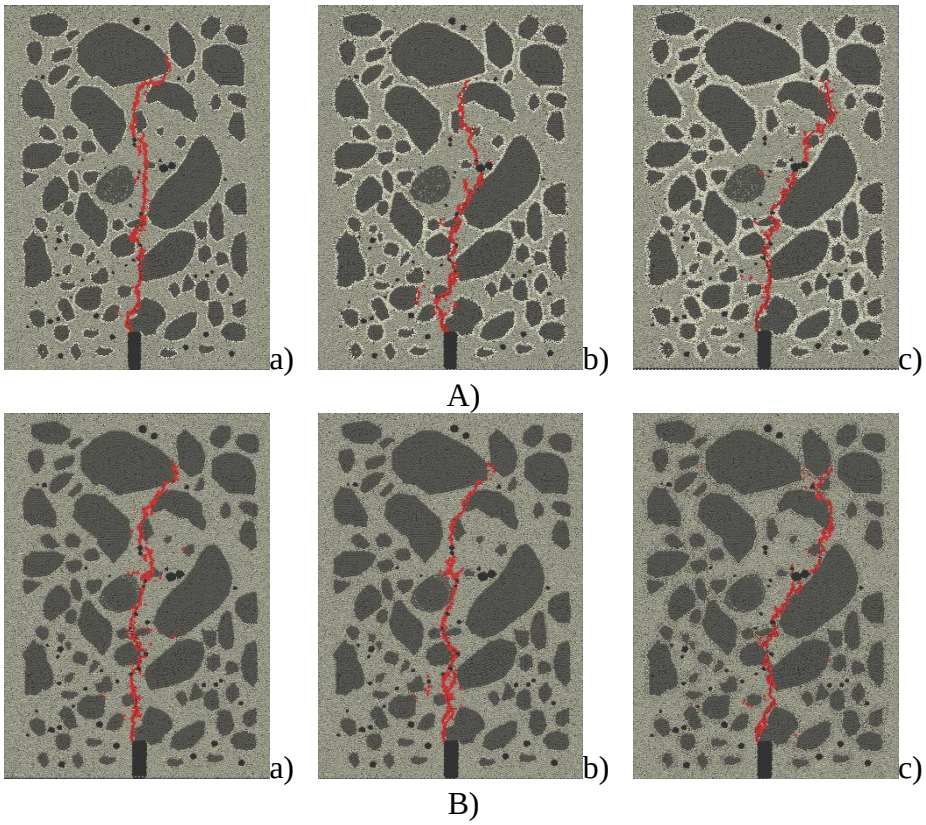

Figure 8: Final crack trajectory in concrete beam above notch after test for CMOD=0.1 mm: A) generation method '1' (ITZ with porosity of 20% for: a) 1 ITZ-layer, b) 2 ITZ-layers and c) 3 ITZ-layers) and B) generation method '2' (ITZ with porosity of 22%: a) 1 ITZ-layer, b) 2 ITZ-layers and c) 3 ITZ-layers) (red colour denotes elements with broken contacts, dark grey - aggregate, light grey – ITZ, grey-cement matrix and black – macro-voids)

6 ACKNOWLEDGEMENT

Research work has been carried out by the authors as a part of the project "*Experimental and numerical analysis of coupled deterministic-statistical size effect in brittle materials*" financed by the National Research Centre NCN (UMO-2013/09/B/ST8/03598).

REFERENCES

[1] Bažant, Z. and Planas, J. 1997. Fracture and size effect in concrete and other quasi-brittle materials. *CRC Press LLC, Boca Raton*.

[2] Lilliu, G. and van Mier, J.G.M. 2003. 3D lattice type fracture model for concrete. *Engineering Fracture Mechanics* 70, 927-941.

[3] Tejchman J. and Bobiński J. 2013. Continuous and discontinuous modelling of fracture in concrete using FEM. *Springer, Berlin-Heidelberg* (eds. W. Wu and R. I. Borja).

[4] Gitman, I. M., Askes, H. and Sluys, L.J. 2008. Coupled-volume multi-scale modelling of quasi-brittle material. *European Journal of Mechanics A/Solids* 27, 302-327.

[5] Skarżyński, Ł. and Tejchman, J. 2010. Calculations of fracture process zones on meso-scale in notched concrete beams subjected to three-point bending. *European Journal of Mechanics A/Solids* 29 (4), 746-760.
[6] Scrivener, K.L., Crumbie, A.K. and Laugesen, P. 2004. The interfacial transition zone (ITZ) between cement paste and aggregate in concrete. *Interface Science* 12, 411-421, Springer Netherlands.
[7] Königsberger, M., Pichler, B. and Hellmich, Ch. 2014. Micromechanics of ITZ-aggregate interaction in concrete Part II: strength upscaling. *Journal of American Ceramic Society. Journal of American Ceramic Society* 97, 543-551.
[8] Kim, S.M. and Abu Al-Rub, R. K. 2011. Meso-scale computational modeling of the plastic-damage response of cementitious composites. *Cement and Concrete Research* 41, 339-358.
[9] Donze, F.V., Magnier, S.A., Daudeville, L. and Mariotti, C. 1999. Numerical study of compressive behaviour of concrete at high strain rates. *Journal for Engineering Mechanics*, 122(80), 1154-1163.
[10] Potyondy, D.O. and Cundall, P. A. 2004. A bonded-particle model for rock. *Int. J. Rock Mechanics and Mining Sciences*. 41(8), 1329-1364.
[11] Dupray, F., Malecot, Y., Daudeville, L. and Buzaud, E. 2009. A mesoscopic model for the behaviour of concrete under high confinement. *International Journal for Numerical and Analytical Methods in Geomechanics* 33, 1407-1423.
[12] Obermayr, M., Dressler, K., Vrettos, C. and Eberhard, P. 2013. A bonded-particle model for cemented sand. *Computers and Geotechnics* 49, 299-313.
[13] Nitka, M. and J. Tejchman, J. 2015. Modelling of concrete behaviour in uniaxial compression and tension with DEM. *Granular Matter* 17, 1, 145-164.
[14] Nitka,M. and Tejchman, J. 2018 A three-dimensional meso-scale approach to concrete fracture based on combined DEM with x-ray micro-CT images. *Cement and Concrete Research*, 107:11-29
[15] Skarżyński, Ł., Nitka, M., and Tejchman, J. 2015 Modelling of concrete fracture at aggregate level using FEM and DEM based on x-ray μCT images of internal structure. *Engineering Fracture Mechanics* 10, 147:13-35.
[16] Suchorzewski, J., Tejchman, J. and Nitka, M. 2017 Experimental and numerical investigations of concrete behaviour at meso-level during quasi-static splitting tension. *Theoretical and Applied Fracture Mechanics*, doi: 10.1016/j.tafmec.2017.10.011.
[17] Kozicki, J. and Donze, F. 2008. A new open-source software developer for numerical simulations using discrete modeling methods. *Computer Methods in Applied Mechanics and Engineering* 197:4429-4443.
[18] Šmilauer, V. and Chareyre, B. 2011. Yade DEM Formulation. Manual.
[19] Skarżyński, Ł., Tejchman, J. 2016. Experimental investigations of fracture process in concrete by means of x-ray micro-computed tomography. *Strain* 52, 26-45, 2016.
[20] Ergenzinger, Ch., Seifried, R. and Eberhard, P. 2011. A discrete element model to describe failure of strong rock in uniaxial compression. *Granular Matter* 13, 341-364.
[21] Cundall, P. A. and Hart, R. 1992. Numerical modelling of discontinua. *Engineering Computations 9*:101-113.